



Geophysical Research Letters

RESEARCH LETTER

10.1029/2018GL081714

Key Points:

- This study conducted a radar climatology of convergence boundaries and their associated convection over a sharp vegetation-contrast area
- Vegetation contrast greatly impacted boundary traits, including location, orientation, length, motion, and diurnal cycle
- Vegetation contrast might modify the occurrence frequency and high-frequency location of boundary-associated convective precipitation

Supporting Information:

- Supporting Information S1
- Figure S1

Correspondence to:

Z. Meng,
zymeng@pku.edu.cn

Citation:

Huang, Y., Meng, Z., Li, W., Bai, L., & Meng, X. (2019). General features of radar-observed boundary layer convergence lines and their associated convection over a sharp vegetation-contrast area. *Geophysical Research Letters*, 46, 2865–2873. <https://doi.org/10.1029/2018GL081714>

Received 19 DEC 2018

Accepted 13 FEB 2019

Accepted article online 15 FEB 2019

Published online 4 MAR 2019

General Features of Radar-Observed Boundary Layer Convergence Lines and Their Associated Convection Over a Sharp Vegetation-Contrast Area

Yipeng Huang^{1,2} , Zhiyong Meng² , Wanbiao Li² , Lanqiang Bai³ , and Xuefeng Meng⁴

¹Laboratory of Straits Meteorology, Xiamen Meteorological Bureau, Xiamen, China, ²Laboratory for Climate and Ocean-Atmosphere Studies, Department of Atmospheric and Oceanic Sciences, School of Physics, Peking University, Beijing, China, ³Center for Monsoon and Environment Research, School of Atmospheric Sciences, and Guangdong Province Key Laboratory for Climate Change and Natural Disaster Studies, Sun Yat-Sen University, Guangzhou, China, ⁴Inner Mongolia Autonomous Region Meteorological Observatory, Hohhot, China

Abstract Boundary layer convergence lines (boundaries), an important trigger of convective storms, can be produced by land surface contrasts. This study explored a five-year summertime radar climatology of boundaries and their associated convection in response to vegetation contrast around the bend of the Yellow River in North China. A total of 323 boundaries were identified with 44% being convection-associated. The boundaries especially the convective boundaries were more frequent over the arid area than those over the vegetated area and tended to have an orientation parallel to the vegetation contrast line. The boundary activities collocated well with the diurnal variation in surface temperature difference across the vegetation contrast. Compared with the nonconvective boundaries, the convective boundaries formed earlier and moved faster into the inner arid area, obtained maximum length around midday, and then initiated convection. Vegetation contrast might also affect the high-frequency location and magnitude of boundary-associated convective precipitation.

Plain Language Summary Boundary layer convergence lines (boundaries) have long been known as an important precursor for convective storms. This study performed a five-year summertime radar climatology of boundaries and their associated convection in response to vegetation contrast (especially irrigation-desert contrast) around the bend of the Yellow River in North China. The results showed that the vegetation contrast significantly impacted the boundary characteristics in terms of location, orientation, maximum length, motion, and diurnal cycle, and might potentially impact the high-frequency location and magnitude of the boundary-associated convective precipitation as well. Compared with the nonconvective boundaries, the convective boundaries showed higher occurrence frequency in arid area, more apparently orientated along the dominant vegetation contrast line, formed and obtained their maximum length earlier, and moved faster into the inner arid area. These features may aid forecasters in evaluating the potential of a boundary in triggering convection.

1. Introduction

Boundary layer convergence lines (referred to as boundaries hereafter), by acting as a lifting mechanism, have long been recognized as an important trigger to convective initiation and development (e.g., Alexander et al., 2018; Byers & Rodebush, 1948; Purdom, 1976; Weckwerth & Parsons, 2006; Wilson & Schreiber, 1986). Boundaries are often manifested as fine lines of clear-air radar echoes (generated by birds, insects, dust, etc.; Wilson et al., 1994). Since convective storms likely occur and develop nearby boundaries, accurately monitoring boundaries can aid forecasters in issuing successful convection nowcasts (e.g., Mueller et al., 2003; Wilson & Mueller, 1993; Roberts et al., 2012).

Boundaries and their associated convective activities often develop as a result of the differential heating due to land surface contrasts (Gambill & Mecikalski, 2011). Some of such land surface contrasts have been well documented in relevant statistical studies, such as mountain-valley contrast (Wilson & Schreiber, 1986), land-sea contrast (Koch & Ray, 1997; Wilson & Megehard, 1997), and land-lake contrast (Alexander et al., 2018; Sills et al., 2011). However, how boundaries and their associated convection respond to vegetation contrast has little been studied. Answering this question is particularly important

for arid/semiarid areas where the vegetation cover keeps changing due to both natural processes (e.g., seasonal cycle; Taylor et al., 2011) and anthropogenic modifications (e.g., desertification, afforestation, and irrigation).

The irrigation area in the bend of the Yellow River and its vicinity in Inner Mongolia, North China (hereafter referred to as Hetao Irrigation District), provides an ideal vegetation contrast (Figures 1a and 1b) for studying boundaries and their associated convection (e.g., Figure 2). Hetao Irrigation District is one of the most extensive irrigations in Asia, and the cultivated land is mainly irrigated by the Yellow River. It is surrounded by wide arid areas, such as deserts. Many long-lasting mesoscale convective systems that had a high impact in East China originated in this area such as those producing the heavy rainfall event in Beijing on 21 July 2012 (Meng et al., 2018) and the downburst in Shangqiu, Henan Province on 3 June 2009 (Bai et al., 2019).

Vegetation impacts on atmospheric processes around Hetao Irrigation District have drawn some attention. Sato et al. (2007) conducted a statistical analysis of satellite images and found that the cloud formation frequency over the irrigation district was lower than that over the surrounding arid area. They speculated that the vegetation contrast might have induced mesoscale circulations, which consequently affected cloud formation around the irrigation district. This speculation was verified by Kawase et al. (2008) through a numerical experiment. However, neither Sato et al. (2007) nor Kawase et al. (2008) have related the vegetation contrast with boundaries or associated convective processes since no radar observations were used in their studies. As visible indicators of vegetation-contrast-induced circulations, radar-observed boundaries can be easily used in operational convection nowcasts. The present study intends to explore the climatology of boundaries and their associated convection in response to vegetation contrast around Hetao Irrigation District based on five-year summertime radar observations.

2. Data and Methods

2.1. Radar-Based Identification of Boundaries and Their Associated Convection

The identification of boundaries and their associated convection was based on reflectivity data collected by the China New Generation Doppler Weather Radar at Linhe (LHRD; 40.73°N, 107.36°E; located at the center of Figure 1a) within Hetao Irrigation District during June–August from 2012 to 2016 with a 95% time coverage. LHRD has a 5.5-cm wavelength (CD band) with a 1° beam width and a 0.25-km radial resolution. Operated in Volume Coverage Pattern 21 mode, LHRD takes approximately 6 min to complete a volume scan which contains nine elevations between 0.5° and 19.5°. The reflectivity data were preprocessed to remove unorganized pixels which may hinder the identification of boundaries and their associated convection (detailed procedures are given in Text S1 in the supporting information). After the data processing, the reflectivity data at each elevation were uniformly interpolated onto a 0.5-km grid.

Boundaries were identified and tracked in successive images of composite reflectivity (the vertical maximum reflectivity of the two lowest elevations of 0.5° and 1.5°). The two lowest elevations instead of all nine elevations were used since boundaries mainly appeared at low levels and the negative effect of high-level non-boundary echoes on boundary location accuracy was minimal (e.g., Figure 2). A boundary was defined in this study as a linear area of enhanced reflectivity with a width less than 10 km according to Koch and Ray (1997), a length greater than 10 km and a duration of at least 6 min based on Wilson and Schreiber (1986). The at-least-6-min duration was required to cover short-lived boundaries that lasted for at least two continuous volume scans. The “enhanced reflectivity” was quantified as -5 to 10 dBZ in most cases or 0 to 10 dBZ when extensive clear-air echoes arose. If a boundary originated from a preexisting convective storm (≥ 30 -dBZ reflectivity), it was classified as a gust front and was excluded.

Three stages in the life cycle of a boundary were identified as follows: (1) boundary formation stage: the first time when the boundary definition was met (e.g., Figure 2a); (2) boundary dissipation stage or convective initiation stage: the last time when a boundary was identified, depending on whether a boundary initiated convection or not. For a nonconvective boundary, the dissipation stage was identified when the boundary definition was met for the last time. For a convective boundary, which was declared when new convective storms with reflectivity exceeding 30 dBZ occurred within 50 km of the boundary, the convective initiation stage (e.g., Figure 2c) rather than dissipation stage was identified when the first 10 dBZ of the first convective storm appeared (10 dBZ rather than 30 dBZ was chosen to prevent the boundary from being apparently

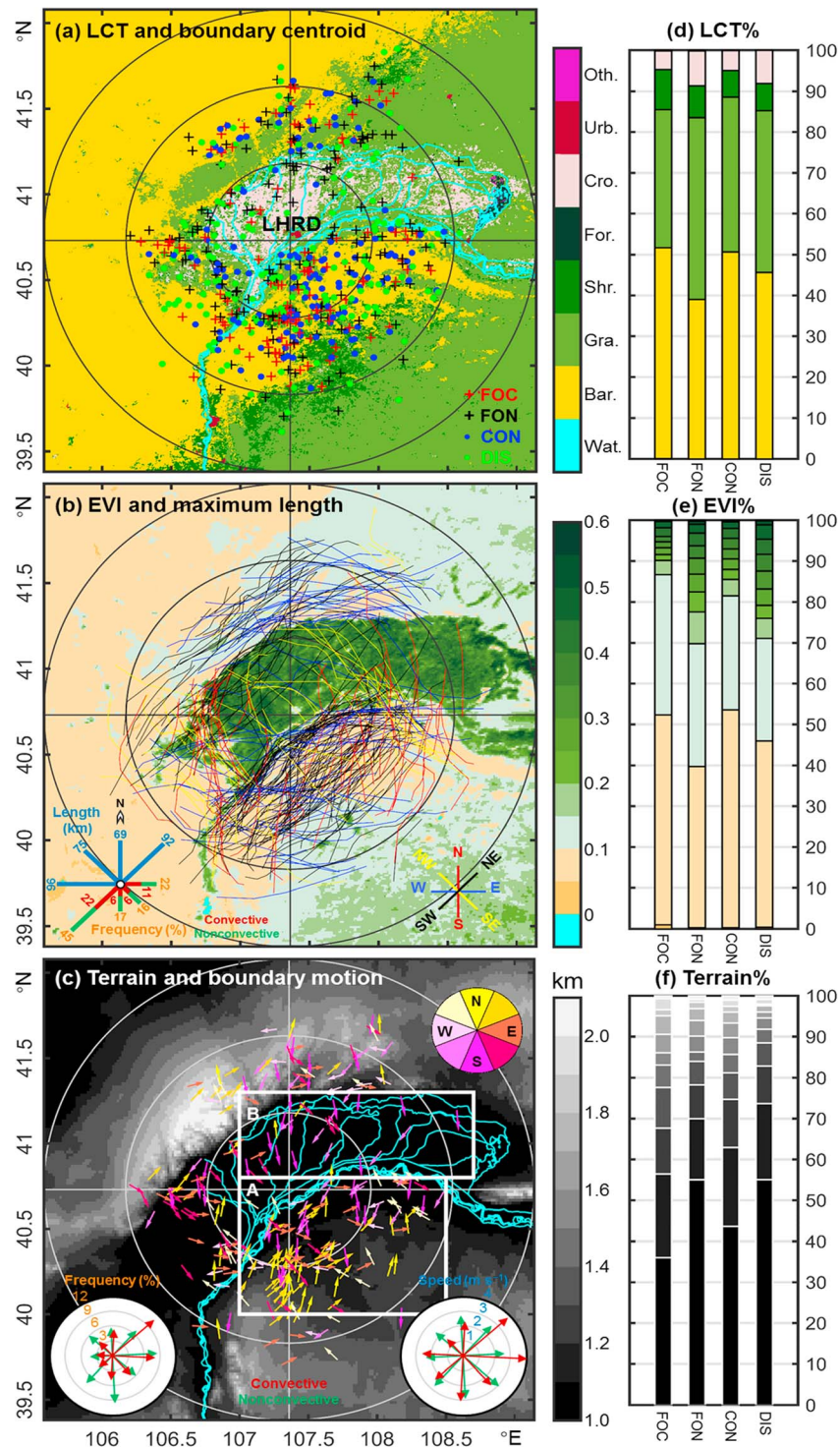


Figure 1. Distributions of (a) centroids of the convective boundaries at the formation (FOC) and convective initiation stages (CON), and the nonconvective boundaries at the formation (FON) and dissipation (DIS) stages, (b) maximum length, and (c) movement of all identified boundaries overlapped with (a) land cover type (LCT), (b) enhanced vegetation index (EVI; 15-month average), and (c) terrain elevation. Also shown are the percentages of boundary lengths over different (d) LCTs, (e) EVI ranges, and (f) terrain elevation ranges. The LCTs in (a) and (d) include water (Wat.), barren or sparsely vegetated (Bar.), grasslands (Gra.), shrublands (Shr.), forests (For.), cropland/natural vegetation mosaic (Cro.), urban and built-up (Urb.), and others (Oth.). The cyan curves in (a) and (c) denote the Yellow River. The mean length (blue) and frequency (orange for all, red for convective, and green for nonconvective) of the boundaries at their maximum length stage for four orientations are shown in the bottom left corner of (b). The frequency and mean speed of the boundaries with a color code similar to that in (b) for different directions of movement are shown in the bottom left and right corners of (c), respectively. The boxes A and B in (c) respectively denote the desert and irrigation areas selected for further analysis in Figure S1 in the supporting information.

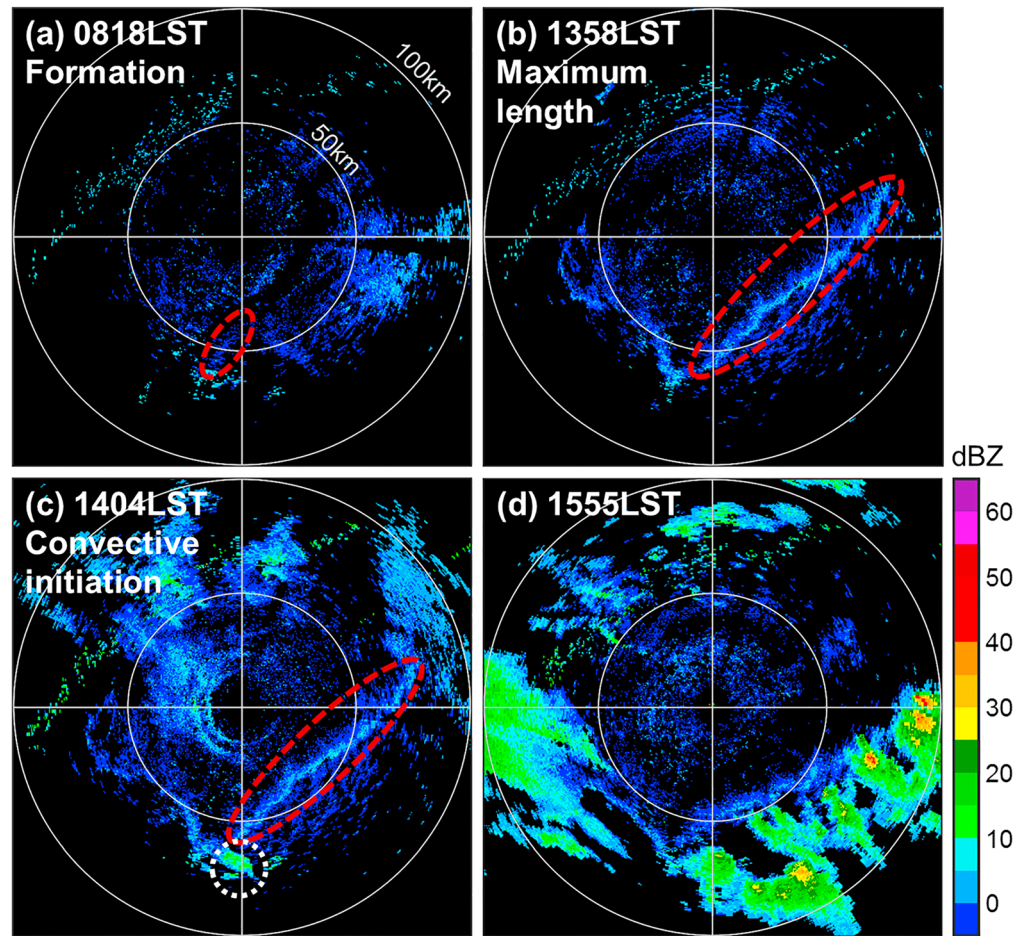


Figure 2. Radar composite reflectivity of a convective boundary on 4 June 2013 based on the (a and b) two lowest elevations and (c and d) all nine elevations. The red circles in (a)–(c) highlight the boundary at its formation, maximum length, and convective initiation stages, respectively. The white circle in (c) highlights the first ≥ 10 -dBZ echo of the first convective storm near the boundary. The central intersections denote the LHRD site, and the range rings are shown at 50-km intervals in gray.

influenced by convection). After the convective initiation stage, the original boundary was generally affected by the convection or mixed with the gust fronts of the convection, thus difficult to be clearly identified, also as the reason why dissipation did not apply; (3) boundary maximum length stage: the stage when a boundary achieved its maximum length between the formation and convective initiation/dissipation stages (e.g., Figure 2b). About 6% of the boundary locations for all three stages could not be obtained due to the missing of radar data, but such a small percentage of missing locations were negligible for the statistical analysis.

The location of boundary-associated convective precipitation was identified for all convective boundaries based on composite reflectivity obtained by excluding the two lowest elevations (0.5° and 1.5°) to avoid low-level clutter that could not be completely removed in the data preprocessing. Such clutter was generally ground and mountain clutter that mainly appeared in the two lowest elevations and had high reflectivity similar to convection. A convective boundary might induce convection at different locations (e.g., Figure 2 d). Boundary-associated convective precipitation was determined when the composite reflectivity of a grid within 50 km of the boundary location exceeded 30 dBZ (Wilson & Schreiber, 1986) within 2 hr from the convective initiation stage. The 2-hr criterion was chosen to focus on convection with a certain developing intensity and the convection that reached 30 dBZ beyond 2 hr from the convective initiation stage was generally too weak.

2.2. Geographical Feature and Surface Temperature Estimation

The land cover product MCD12Q1 from Moderate Resolution Imaging Spectroradiometer (MODIS) was used to generate eight primary classes of land cover in the study area in a 0.005° grid of longitude and latitude (Figure 1a). MODIS-enhanced vegetation index (EVI) product MOD13A3 from June to August in 2012–2016 was bilinearly interpolated onto a 0.01° grid of longitude and latitude for each month. Terrain elevation data were adopted from the ETOPO1 data set in a 1-arc-min grid produced by the National Geophysical Data Center (Amante & Eakins, 2009). Detailed procedures in generating the land cover, EVI, and terrain height are given in Text S2 in the supporting information. The irrigation district is mainly covered by cropland and lush grassland and thus has a significantly higher EVI than its surrounding area which is mostly desert and sparse grassland (Figures 1a and 1b). The terrain height variability is relatively gentle between the irrigation district and its surrounding arid area, except in the northwest mountain area (Figure 1c).

The monthly-averaged hourly surface temperatures of vegetated area ($EVI > 0.3$) and arid area ($EVI < 0.15$) and their differences were estimated by using infrared ($10.4 \mu\text{m}$) brightness temperature data from June to August in 2016 from Himawari-8, the Japanese new-generation geostationary satellite. The detailed procedures are given in Text S3 in the supporting information.

3. Statistical Features of Boundaries and Their Relation With the Vegetation Contrast

During the five summers from 2012 to 2016, a total of 323 radar-observed boundaries were identified around Hetao Irrigation District, and 44% (143) of which were convective boundaries.

3.1. Geographical Distribution

The identified boundaries were less frequent over the irrigation district than those over the surrounding area (Figure 1a). This result was consistent with Sato et al. (2007) and Kawase et al. (2008). As suggested in their studies, around the irrigation district where the terrain is gentle, the sharp vegetation contrast alone can cause prominent surface temperature contrast and thus induce thermal circulations. In the northwest mountain area, the vegetation-contrast-induced circulation may enhance the mountain-valley circulation (Kawase et al., 2008). Kawase et al. (2008) showed that the upward and downward flows of the vegetation-contrast-induced circulation are located in the warm arid area and the cold vegetated area, respectively. The upward flow is associated with surface convergence and thus favors the frequent occurrence of radar-observed boundaries over the arid area (especially the southeast desert) rather than over the vegetated area.

The roles of vegetation contrast in the geographical distributions of the boundaries were quantified by calculating the percentages of boundary lengths over different land cover types, EVI ranges, and terrain elevation ranges. In all different stages, more than 80% of the boundary lengths were located in barren area and grasslands, while less than 10% appeared in cropland which is the primary land cover of the irrigation district (Figures 1a and 1d). In terms of EVI, over 70% of the boundary lengths were detected where the EVI was less than 0.15, while less than 20% were detected where the EVI was greater than 0.3; this distribution was consistent for different stages (Figure 1e). Evidently, the observed boundaries tended to occur in the arid side of vegetation contrast. Considering that over 70% of boundary lengths were concentrated over the gentle terrain with terrain elevations between 1.0 and 1.4 km (Figures 1c and 1f), the formation of boundaries was mainly associated with vegetation contrast rather than terrain variation, which is consistent with the dominant role of the vegetation contrast in inducing thermal circulations in this area (Kawase et al., 2008; Sato et al., 2007).

The arid-area-dependence feature of boundary length distribution was more distinct for the convective boundaries than the nonconvective boundaries, although there was no apparent difference in the distribution of their centroids (Figure 1a). The percentage of the lengths of convective boundaries over arid area (i.e., barren and sparsely vegetated area in Figure 1d or $EVI < 0.15$ area in Figure 1e) was ~10–15% higher than that of the nonconvective boundaries at the formation stage (the first two columns in Figures 1d and 1e).

3.2. Boundary Orientation

Boundaries tended to orient along the dominant vegetation contrast line whose orientation is mainly NE–SW and E–W (Figure 1b). More boundaries at their maximum length stage were found to parallel to the dominant vegetation contrast line (45% of NE–SW and 22% of E–W orientations), along with a mean maximum length longer than 90 km (Figure 1b). These longer boundaries mainly appeared in the arid areas to the southeast and northwest of the central irrigation district.

Compared with the nonconvective boundaries, the convective boundaries more apparently oriented along the dominant vegetation contrast line (Figure 1b). About half of the boundaries parallel to the dominant contrast line (NE–SW and E–W orientations) were convective, while more than 60% of the boundaries perpendicular to the dominant vegetation contrast line (N–S and NW–SE orientations) were nonconvective (Figure 1b). Along the dominant vegetation contrast line, the stronger cross-line circulations may lead to stronger surface convergence and thus may increase the likelihood of a boundary becoming convective.

3.3. Boundary Motion

The boundary motion was investigated in terms of the movement of boundary centroid from the formation stage to maximum length stage. The vegetation-contrast-induced circulations generally blow from the vegetated area to the surrounding arid area at lower levels (Kawase et al., 2008; Sato et al., 2007). As a result, the boundaries over the southeast desert (region A in Figure 1c) tended to move into the inner arid area from different directions (Figure S1a in the supporting information). Over the irrigation district (region B in Figure 1c), by contrast, the boundaries did not converge but had a dominantly southward component of movement (Figure S1b in the supporting information). The mean speed of movement of all boundaries was 2.9 m/s.

Over the whole area, the convective boundaries moved to the northeast and east more frequently at a faster speed (~ 4 m/s) than to other directions, while the nonconvective boundaries were more isotropic in both frequency and speed (the inner compass plots in Figure 1c). The faster movement of convective boundaries toward northeast and east could be partly due to a more favorable environmental wind that had a direction similar to that of the boundary movement. The movement features of convective and nonconvective boundaries over the southeast desert were similar to those over the whole area due to its dominant sample size, except that the higher frequency and faster movements of convective boundaries were more dominant in the northeastward direction (Figure S1a in the supporting information). Over the irrigation district where the nonconvective boundaries were dominant, both the convective and nonconvective boundaries mainly moved southward with the convective boundaries having a faster speed (Figure S1b in the supporting information).

3.4. Diurnal Cycle

Boundary frequencies at different stages show apparent diurnal variations (Figure 3a). More than 80% of the boundaries formed during the daylight time between 08 and 16 local standard time (LST = UTC + 8 hr), with a late-morning peak at 10–11 LST. A majority of the boundaries obtained their maximum length in the early afternoon peaking at 12–13 LST. The peak of convective initiation happened also at 12–13 LST. Approximately 70% of the nonconvective boundaries dissipated in the evening between 17 and 21 LST.

The convective boundaries formed and obtained their maximum length overall earlier than the nonconvective boundaries (Figure 3a). The formation peak time of convective boundaries was 10–11 LST, which was about 1 hr ahead of the formation peak time of nonconvective boundaries. Most convective boundaries obtained their maximum length around midday (11–14 LST) and then began to initiate convection, while most nonconvective boundaries achieved their maximum length about 3 hr later during the afternoon between 13 and 18 LST. This result suggests that the boundaries with an earlier formation time more likely became a convective boundary.

The diurnal cycles of boundary activities collocated well with the diurnal variation in the land surface temperature contrast between the arid (EVI < 0.15) and vegetated (EVI > 0.3) areas (Figure 3). The surface temperatures of the arid and vegetated areas were both modulated by solar heating, but the diurnal variability in the arid area was much more significant than that in the vegetated area. This led to an obvious diurnal variation in the surface temperature difference between the arid and vegetated areas and, thus, the diurnal

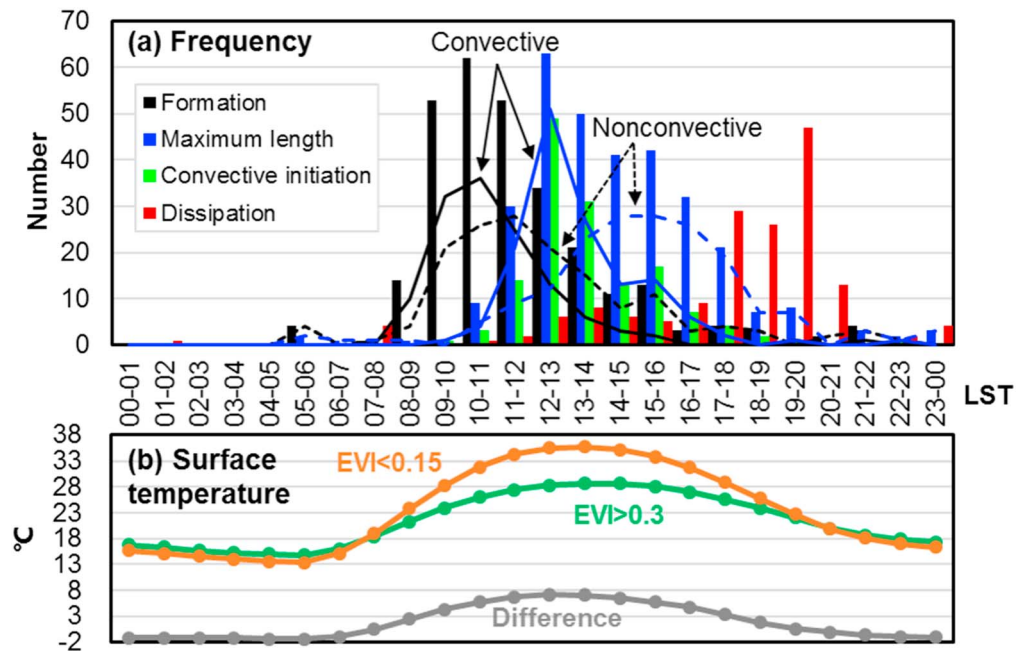


Figure 3. Diurnal cycles (in LST; LST = UTC + 8 hr) of (a) boundary frequency at different stages (bars) and (b) mean surface temperatures (three-month average) in the arid (EVI < 0.15) and vegetated (EVI > 0.3) areas and their difference. The curves in (a) denote the frequency of convective (solid) and nonconvective boundaries (dashed) at the formation (black) and maximum length (blue) stages.

variation in the induced thermal circulation. During the daylight time, the arid area was much warmer than the vegetated area, and the temperature difference reached ~ 3 °C (Figure 3b) at 08 LST, after which boundaries began to form substantially, likely due to the enhanced upward branch of the thermal circulation. The temperature difference reached its maximum (7–8 °C in Figure 3b) at 12–13 LST, corresponding to the peak time of maximum length stage and convective initiation stage of the boundaries. After 17–18 LST, the remarkable temperature difference began to decline, and a large number of the nonconvective boundaries dissipated.

4. Potential Impact of Vegetation Contrast on Boundary-Associated Convective Precipitation

The frequency of convective precipitation associated with a certain convective boundary was computed at each grid as the times when convective precipitation was detected over the 2-hr period starting from the convective initiation stage. The frequency was then normalized by the total scan times of LHRD available in the 2-hr period considering the scan times might slightly change for different boundaries. Finally, the frequencies of all convective boundaries detected during June–August from 2012 to 2016 were accumulated to produce the general distribution map of boundary-associated convective precipitation.

The results showed that the high-frequency location of boundary-associated convective precipitation appeared in the transition zone from the desert to the vegetated areas, which was 50–100 km to the southeast of the radar site (Figure 4a). In Figure 4, an EVI value of 0.125 is used to represent the vegetation transition zone from the desert (EVI < 0.1) to vegetated (EVI > 0.15) areas, and the vegetated side is denoted by the white dots with an EVI value greater than 0.125. The high-frequency location of convective precipitation possibly resulted from the fact that boundary-associated convection mainly occurs when boundaries encounter moisture near the vegetation transition zone. The evapotranspiration over the vegetated side of the transition zone likely acts as a moisture source (Imamovic et al., 2017; Sato et al., 2007; Taylor et al., 2011). Because the area around the irrigation district was more barren and there was less moisture in June than in July and August, the overall convective precipitation frequency in June was lower (Figures 4b–4d). Interestingly, the high-frequency location of convective precipitation migrated slightly northwestward from June to July and August (Figures 4b–4d). This migration occurred possibly because

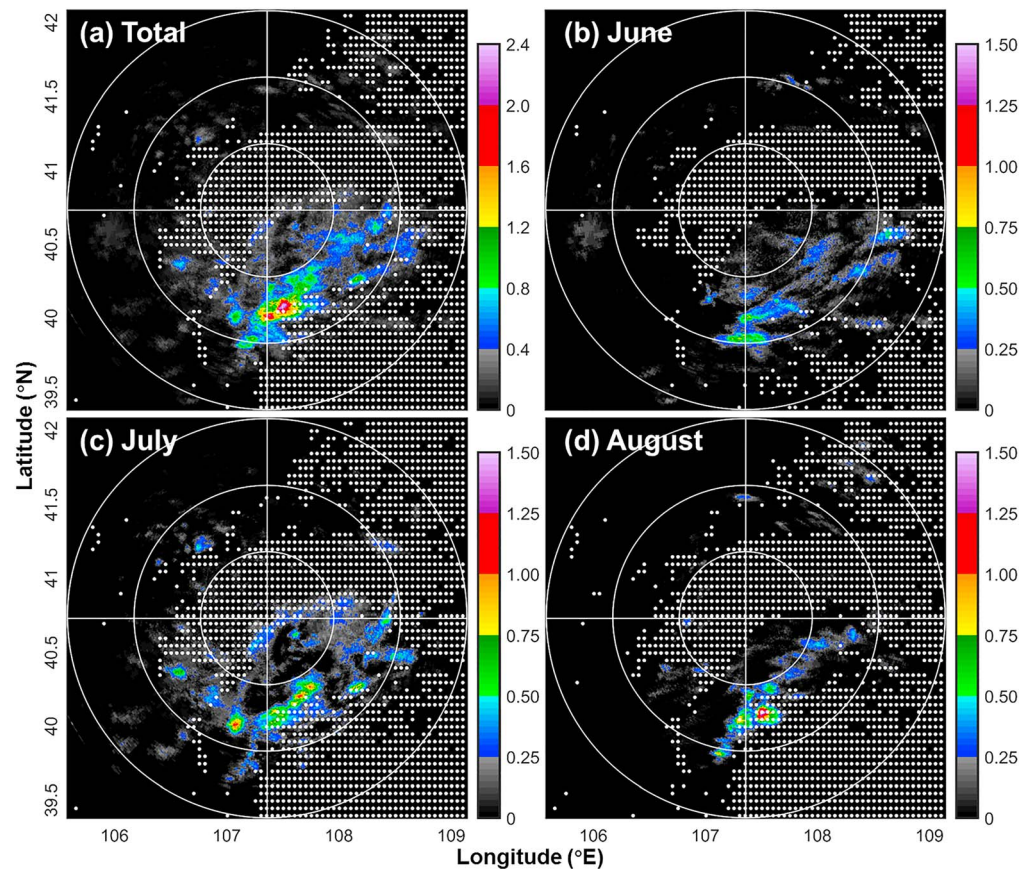


Figure 4. Spatial distributions of the accumulated frequency of boundary-associated convective precipitation in (a) the whole three months of June, July, and August and only (b) June, (c) July, and (d) August. The white dots denote the area with an EVI (five-year average) greater than 0.125.

the area to the southeast of the convective precipitation area was increasingly less barren and the vegetation transition zone (the white dots in Figures 4b–4d) was increasingly closer to the radar site from June to July and August.

5. Conclusions

A five-year summertime radar climatology study was conducted over Hetao Irrigation District in Inner Mongolia, China, where there is a sharp vegetation contrast, to examine how the boundaries and their associated convection respond to the vegetation contrast.

A total of 323 boundaries were identified based on radar data during the study period, 44% of which were convective. The sharp vegetation contrast had a substantial impact on the boundary activities. The identified boundaries dominantly appeared on the warmer arid side rather than the colder vegetated side of the vegetation contrast, with a dominant orientation along the vegetation contrast line. Along the dominant orientation of the vegetation contrast, more boundaries developed with longer maximum lengths. The diurnal cycles of boundary activities collocated well with the surface temperature difference across the vegetation contrast. In general, the boundaries formed after the early morning when the surface temperature difference became apparent. The boundaries obtained their maximum length and began to initiate convection during the early afternoon corresponding to the largest temperature difference. The nonconvective boundaries finally dissipated at nighttime when the temperature difference declined.

Compared with the nonconvective boundaries, the convective boundaries showed greater distinct location dependence on arid area, more apparently orientated along the dominant vegetation contrast line, formed

and obtained their maximum length earlier, and moved mainly northeastward and eastward into the inner arid area at a higher speed. The convective boundaries caused a high-frequency occurrence of convective precipitation in the transition zone between the arid area and the vegetated area to the southeast of Hetao Irrigation District. This high-frequency zone migrated northwestward from June to July and August with an increasing magnitude.

Acknowledgments

This work was sponsored by the National Natural Science Foundation of China (Grants 41425018 and 41675047) and the Ministry of Science and Technology of China (Grant 2013CB430104). Radar data were provided by the National Meteorological Information Center of the China Meteorological Administration (<http://www.cma.gov.cn/2011qxw/2011qsjgx/>). The MODIS data were downloaded from NASA's Earth Observing System Data and Information System (EOSDIS; <https://search.earthdata.nasa.gov/search>). The Himawari-8 data were downloaded from the P-Tree system of the Japan Aerospace Exploration Agency (JAXA) at <https://www.eorc.jaxa.jp/ptree/index.html>. All authors of this manuscript do not have a conflict of interest to declare. We thank the Editor and two anonymous reviewers for their constructive comments.

References

- Alexander, L. S., Sills, D. M., & Taylor, P. A. (2018). Initiation of convective storms at low-level mesoscale boundaries in southwestern Ontario. *Weather and Forecasting*, *33*(2), 583–598. <https://doi.org/10.1175/WAF-D-17-0086.1>
- Amante, C., & Eakins, B. (2009). ETOPO1 1 arc-minute global relief model: Procedures, data sources and analysis. NOAA Tech. Memo. NESDIS NGDC-24, NOAA NGDC. <https://doi.org/10.7289/V5C8276M>
- Bai, L., Meng, Z., Huang, Y., Zhang, Y., Niu, S., & Su, T. (2019). Convection initiation resulting from the interaction between a quasi-stationary dryline and intersecting gust fronts: A case study. *Journal of Geophysical Research: Atmospheres*, *124*. <https://doi.org/10.1029/2018JD029832>
- Byers, H. R., & Rodebush, H. R. (1948). Causes of thunderstorms of the Florida peninsula. *Journal of Meteorology*, *5*(6), 275–280. [https://doi.org/10.1175/1520-0469\(1948\)005<0275:COTOTF>2.0.CO;2](https://doi.org/10.1175/1520-0469(1948)005<0275:COTOTF>2.0.CO;2)
- Dwyer, J., & Schmidt, G. (2006). *The MODIS Reprojection Tool. Earth science satellite remote sensing* (pp. 162–177). Berlin, Heidelberg: Springer. https://doi.org/10.1007/978-3-540-37294-3_9
- Gambill, L. D., & Mecikalski, J. R. (2011). A satellite-based summer convective cloud frequency analysis over the southeastern United States. *Journal of Applied Meteorology and Climatology*, *50*(8), 1756–1769. <https://doi.org/10.1175/2010JAMC2559.1>
- Imamovic, A., Schlemmer, L., & Schär, C. (2017). Collective impacts of orography and soil-moisture on deep convection. *Geophysical Research Letters*, *44*, 11,682–11,691. <https://doi.org/10.1002/2017GL075657>
- Kawase, H., Yoshikane, T., Hara, M., Kimura, F., Sato, T., & Ohsawa, S. (2008). Impact of extensive irrigation on the formation of cumulus clouds. *Geophysical Research Letters*, *35*, L01806. <https://doi.org/10.1029/2007GL032435>
- Koch, S. E., & Ray, C. A. (1997). Mesoanalysis of summertime convergence zones in central and eastern North Carolina. *Weather and Forecasting*, *12*(1), 56–77. [https://doi.org/10.1175/1520-0434\(1997\)012<0056:MOSCZI>2.0.CO;2](https://doi.org/10.1175/1520-0434(1997)012<0056:MOSCZI>2.0.CO;2)
- Meng, Z., Tang, X., Yue, J., Bai, L., & Huang, L. (2018). Impact of EnKF surface and rawinsonde data assimilation on the simulation of the extremely heavy rainfall in Beijing on 21 July 2012. *Acta Scientiarum Naturalium Universitatis Pekinensis* (in Chinese with English Abstract), *55*.
- Mueller, C., Saxen, T., Roberts, R., Wilson, J., Betancourt, T., Dettling, S., Oien, N., et al. (2003). NCAR Auto-Nowcast System. *Weather and Forecasting*, *18*(4), 545–561. [https://doi.org/10.1175/1520-0434\(2003\)018<0545:NAS>2.0.CO;2](https://doi.org/10.1175/1520-0434(2003)018<0545:NAS>2.0.CO;2)
- Purdum, J. F. W. (1976). Some uses of high resolution GOES imagery in the mesoscale forecasting of convection and its behavior. *Monthly Weather Review*, *104*(12), 1474–1483. [https://doi.org/10.1175/1520-0493\(1976\)104<1474:SUOHRG>2.0.CO;2](https://doi.org/10.1175/1520-0493(1976)104<1474:SUOHRG>2.0.CO;2)
- Roberts, R. D., Anderson, A. R., Nelson, E., Brown, B. G., Wilson, J. W., Pocerlich, M., & Saxen, T. (2012). Impacts of forecaster involvement on convective storm initiation and evolution nowcasting. *Weather and Forecasting*, *27*(5), 1061–1089. <https://doi.org/10.1175/WAF-D-11-00087.1>
- Sato, T., Kimura, F., & Hasegawa, A. S. (2007). Vegetation and topographic control of cloud activity over arid/semiarid Asia. *Journal of Geophysical Research*, *112*, D24109. <https://doi.org/10.1029/2006JD008129>
- Sills, D. M. L., Brook, J. R., Levy, I., Makar, P. A., Zhang, J., & Taylor, P. A. (2011). Lake breezes in the southern Great Lakes region and their influence during BAQS-Met 2007. *Atmospheric Chemistry and Physics*, *11*, 7955–7973. <https://doi.org/10.5194/acp-11-7955-2011>
- Taylor, C. M., Gounou, A., Guichard, F., Harris, P. P., Ellis, R. J., Couvreur, F., & De Kauwe, M. (2011). Frequency of Sahelian storm initiation enhanced over mesoscale soil-moisture patterns. *Nature Geoscience*, *4*(7), 430–433. <https://doi.org/10.1038/ngeo1173>
- Weckwerth, T. M., & Parsons, D. B. (2006). A review of convection initiation and motivation for IHOP_2002. *Monthly Weather Review*, *134*(1), 5–22. <https://doi.org/10.1175/MWR3067.1>
- Wilson, J. W., & Meigenhardt, D. L. (1997). Thunderstorm initiation, organization, and lifetime associated with Florida boundary layer convergence lines. *Monthly Weather Review*, *125*(7), 1507–1525. [https://doi.org/10.1175/1520-0493\(1997\)125<1507:TIOALA>2.0.CO;2](https://doi.org/10.1175/1520-0493(1997)125<1507:TIOALA>2.0.CO;2)
- Wilson, J. W., & Mueller, C. K. (1993). Nowcasts of thunderstorm initiation and evolution. *Weather and Forecasting*, *8*(1), 113–131. [https://doi.org/10.1175/1520-0434\(1993\)008<0113:NOTIAE>2.0.CO;2](https://doi.org/10.1175/1520-0434(1993)008<0113:NOTIAE>2.0.CO;2)
- Wilson, J. W., & Schreiber, W. E. (1986). Initiation of convective storms by radar-observed boundary layer convergent lines. *Monthly Weather Review*, *114*, 2516–2536. [https://doi.org/10.1175/1520-0493\(1986\)114<2516:IOCSAR>2.0.CO;2](https://doi.org/10.1175/1520-0493(1986)114<2516:IOCSAR>2.0.CO;2)
- Wilson, J. W., Weckwerth, T. M., Vivekanandan, J., Wakimoto, R. M., & Russell, R. W. (1994). Boundary layer clear-air radar echoes: Origin of echoes and accuracy of derived winds. *Journal of Atmospheric and Oceanic Technology*, *11*(5), 1184–1206. [https://doi.org/10.1175/1520-0426\(1994\)011<1184:BLCARE>2.0.CO;2](https://doi.org/10.1175/1520-0426(1994)011<1184:BLCARE>2.0.CO;2)